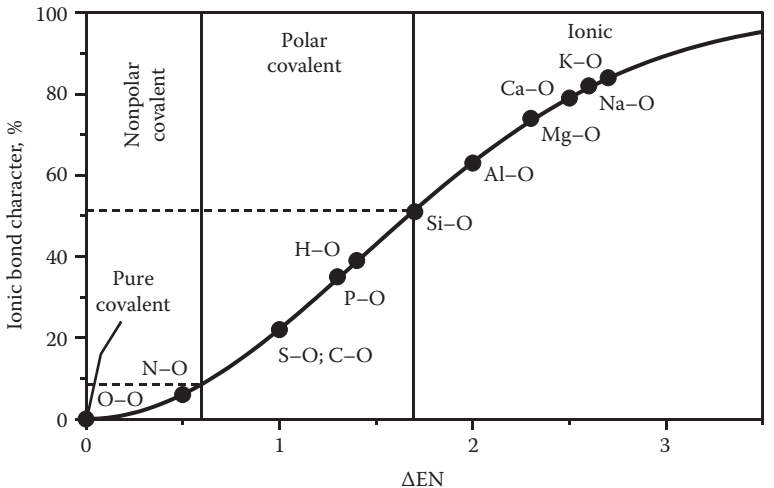


**Figure 2.1** The ionic and covalent character of metal–oxygen bonds as a function of the absolute difference between the metal and oxygen electronegativities (ΔEN). The curve represents the equation: % ionic character = $[1 - \exp(-0.25 \times \Delta EN^2)] \times 100$, which was developed by Linus Pauling to describe bond character.

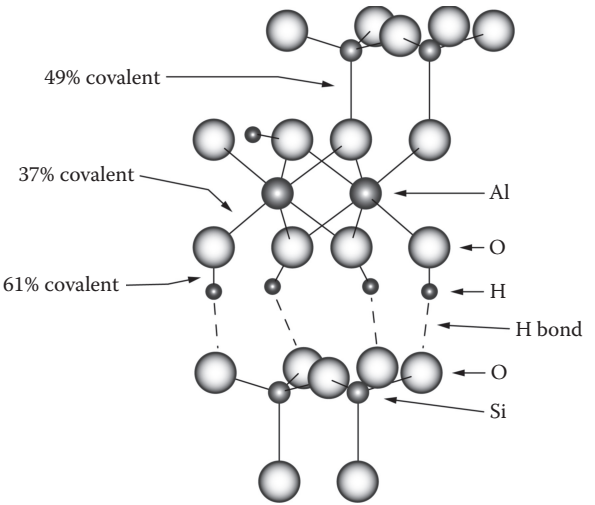


**Figure 2.2** The bonding structure in kaolinite. The Si–O bonds in the Si tetrahedra are 49% covalent. The apical Si tetrahedral oxygen atoms are shared with Al in octahedral coordination (37% covalent bond). The resulting unit, the planar Si tetrahedral sheet and the planar Al octahedral sheet, is the basic 1:1 structural unit of kaolinite. The 1:1 units are connected through hydrogen bonds between basal Si oxygen atoms and Al-bound hydroxyls.

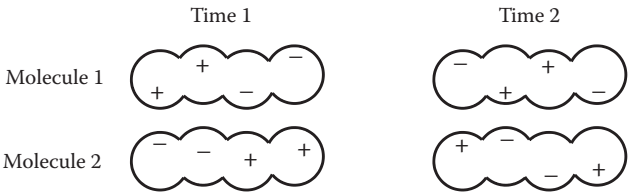


**Figure 2.3** The electron correlation effect that results in van der Waals bonding of two uncharged molecules at time 1 and time 2.

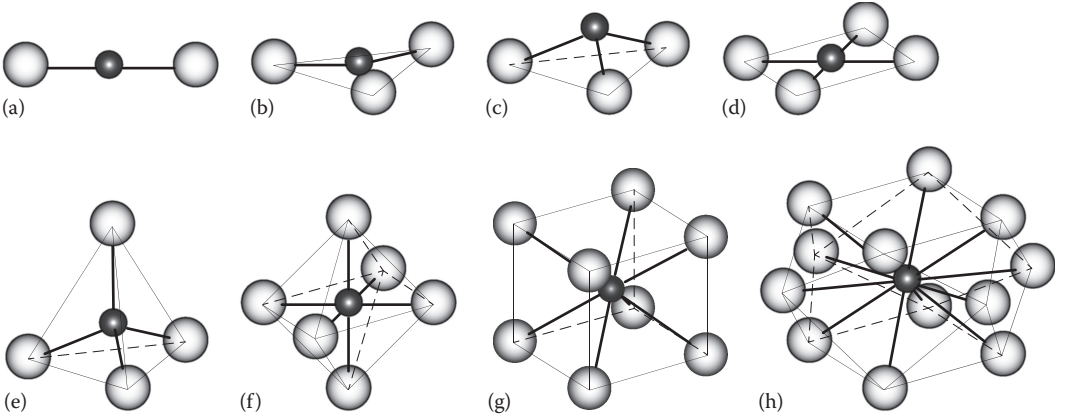


**Figure 2.4** Examples of coordinated structures that occur in soil minerals. The dark circles represent the central metal cations and the light circles are the coordinating anions: (a) linear 2-coordination, (b) planar triangular 3-coordination, (c) trigonal pyramidal 3-coordination, (d) planar square 4-coordination, (e) tetrahedral 4-coordination, (f) octahedral 6-coordination, (g) cubic 8-coordination, and (h) cubooctahedral 12-coordination.

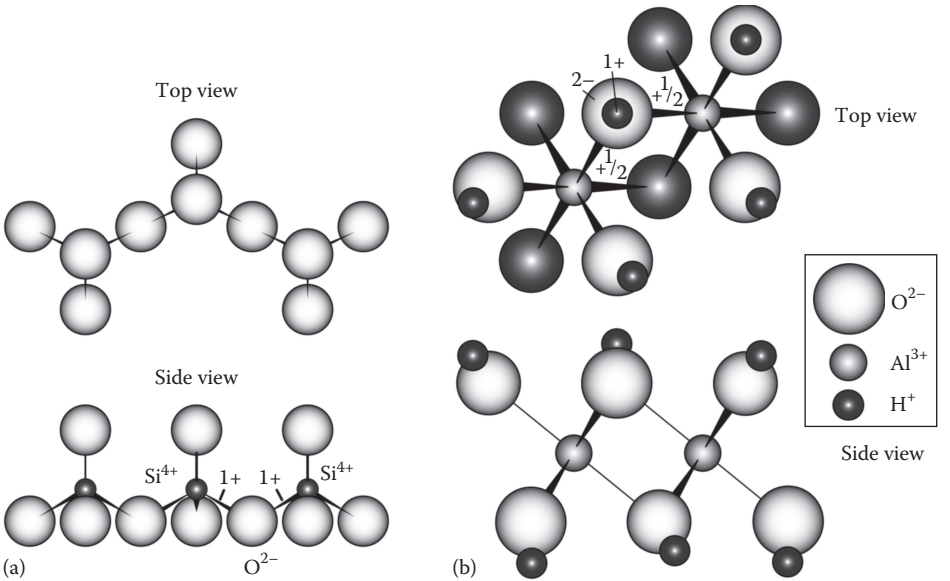


**Figure 2.5** An illustration of Pauling's rule 2: (a) The linkage of silica tetrahedra through basal oxygen atoms. Each bond radiating from a $Si^{4+}$ atom has strength of +1. Therefore, each $O^{2-}$ anion can only bond to two $Si^{4+}$ atoms. (b) The linkage of aluminum octahedra through hydroxide anions. Each bond radiating from an $Al^{3+}$ atom has strength of +½. The single negative charge of the hydroxide anion can be satisfied by two $Al^{3+}$ atoms (alternatively, the –2 charge of the hydroxyl oxygen is satisfied by the +1 of a proton and the two $Al^{3+}$ atoms).

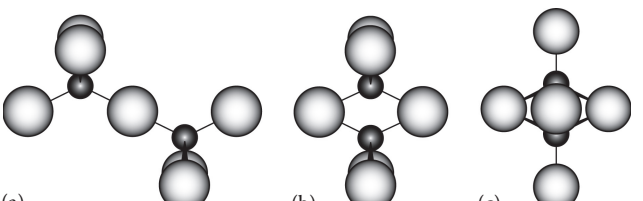


**Figure 2.6** (a) Corner-, (b) edge-, and (c) face-sharing tetrahedral polyhedron linkages. Note that the central metal cations move closer together as the number of shared elements increases.

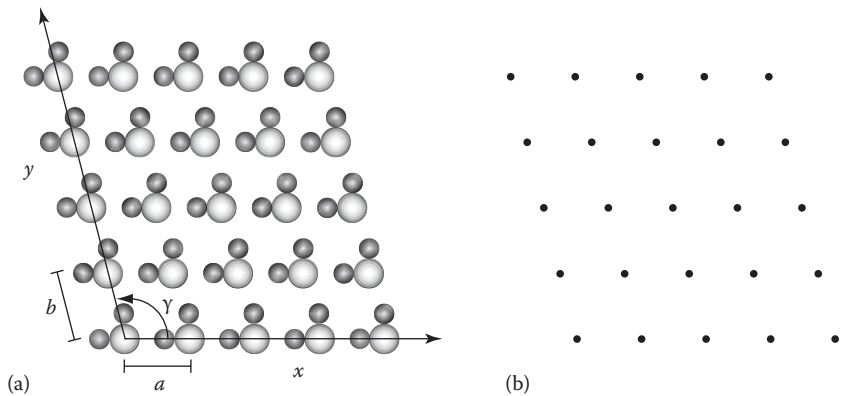


**Figure 2.7** (a) A 2D array of groups of atoms and (b) a plane lattice of points. The 2D structure is defined by the repeat interval of distance $a$ along the $x$-axis; the repeat interval of distance $b$ along the $y$-axis; and the angle, $\gamma$, between the $x$- and $y$-axes.

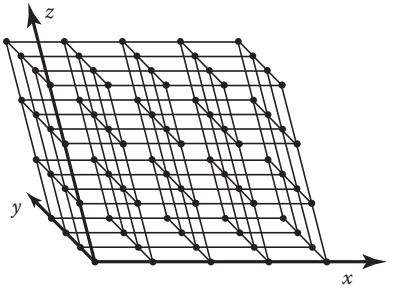


**Figure 2.8** A space lattice of points.

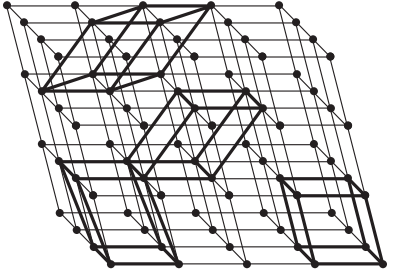

**Figure 2.9** Possible unit cell configurations for a space lattice.

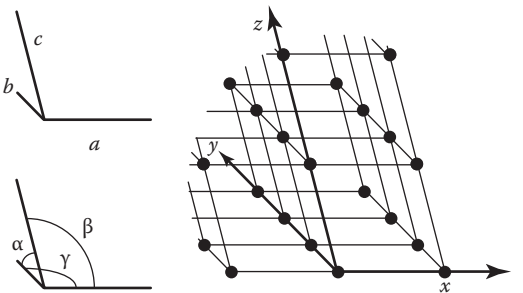


**Figure 2.10** The unit cell is defined by parameters *a*, *b*, and *c* (the *x*-, *y*-, and *z*-dimensions of the unit cell) and the angles α, β, and γ where α is the angle between the *b*- and *c*-axes; β is the angle between the *a*- and *c*-axes; and γ is the angle between the *a*- and *b*-axes.

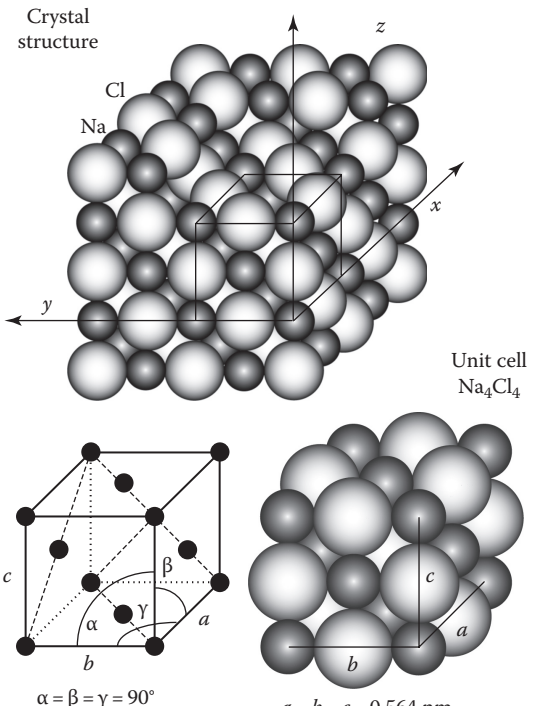


**Figure 2.11** The halite (NaCl) lattice and unit cell.

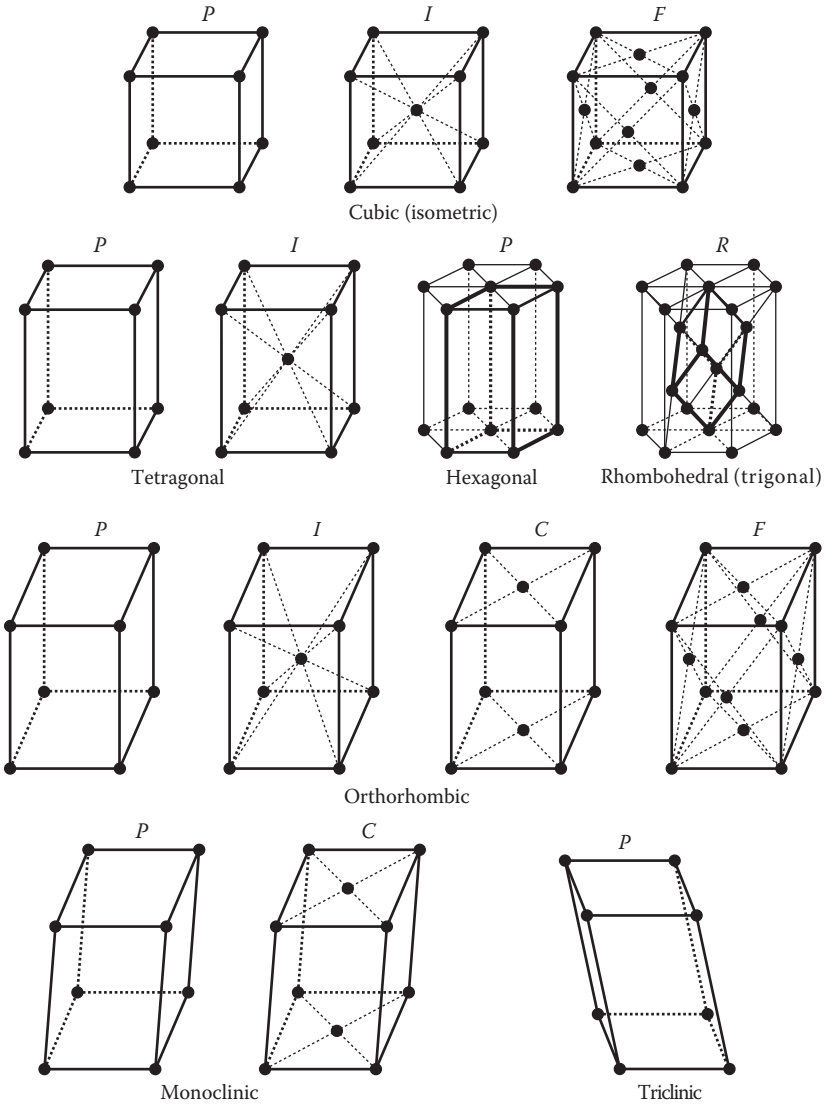


**Figure 2.12** The 14 Bravais lattice types. The lattice parameters and structural characteristics of each lattice type are described in Table 2.4.

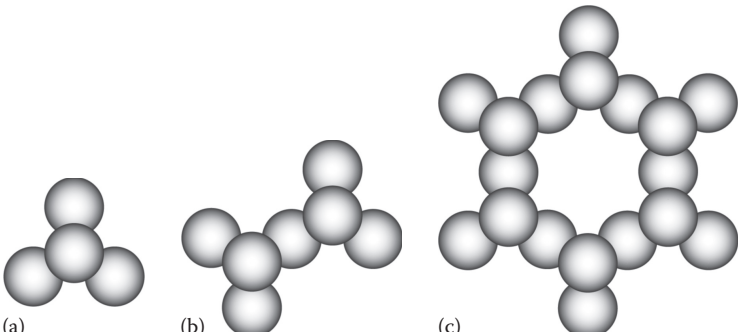


**Figure 2.13** The basic silica tetrahedral units of the (a) nesosilicate, (b) sorosilicate, and (c) cyclosilicate (six-membered ring) minerals.

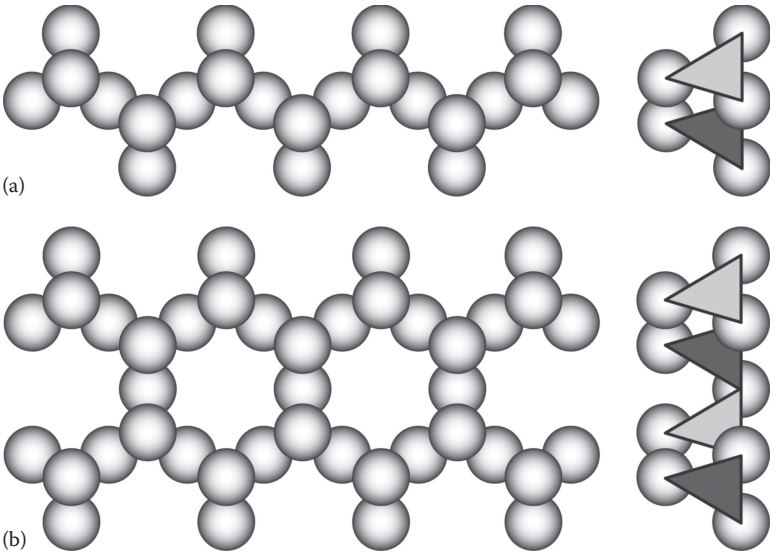


**Figure 2.14** The basic silica tetrahedral units of the (a) single-chain (pyroxenes) and (b) double-chain (amphiboles) inosilicate minerals.

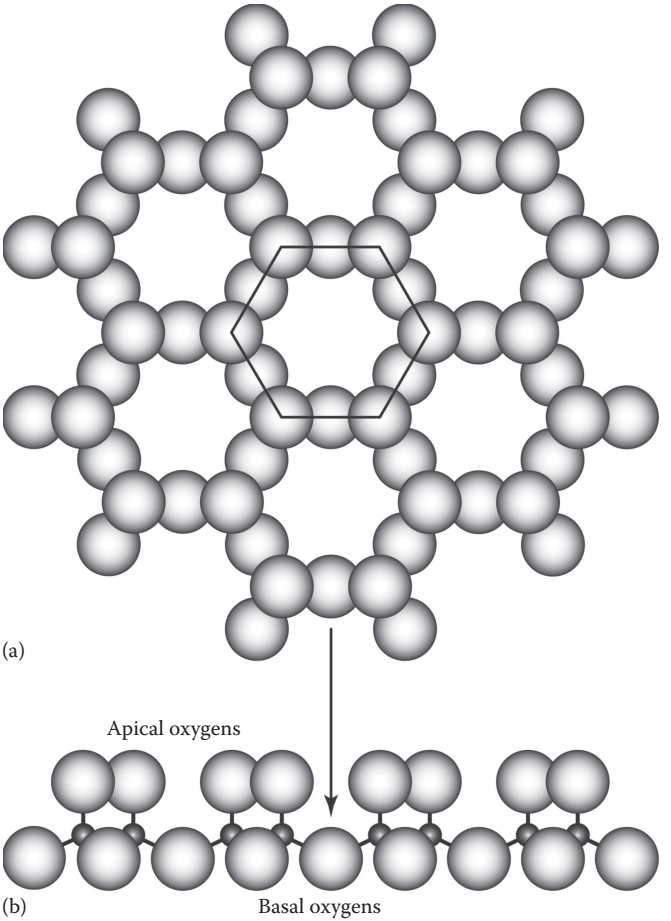


**Figure 2.15** (a) Top and (b) side views of the idealized silica tetrahedral unit (silica sheet) of the phyllosilicate minerals. The arrow correlates a basal oxygen atom in the top and side views.

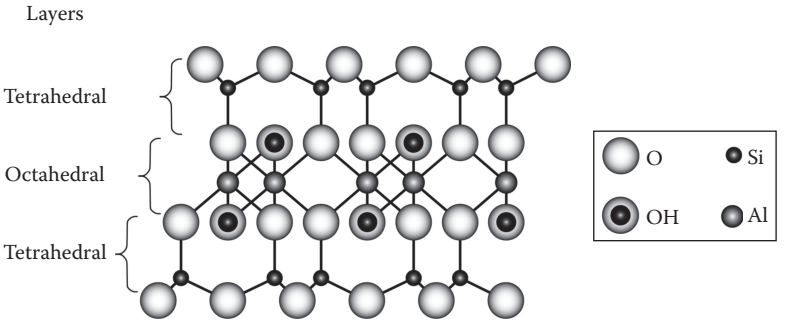


**Figure 2.16** A side view of the 2:1 unit structure of a dioctahedral mica mineral. Note that the apical oxygen atoms of the silica (tetrahedral) layer are also coordinating aluminum in the octahedral layer.

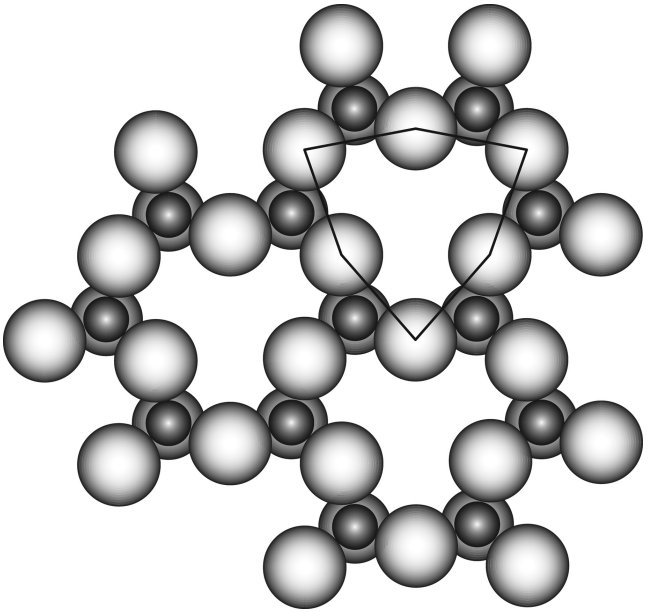

**Figure 2.17** Top view of the tetrahedral sheet of phyllosilicate minerals illustrating the rotation of the individual silica tetrahedra and the ditrigonal symmetry.

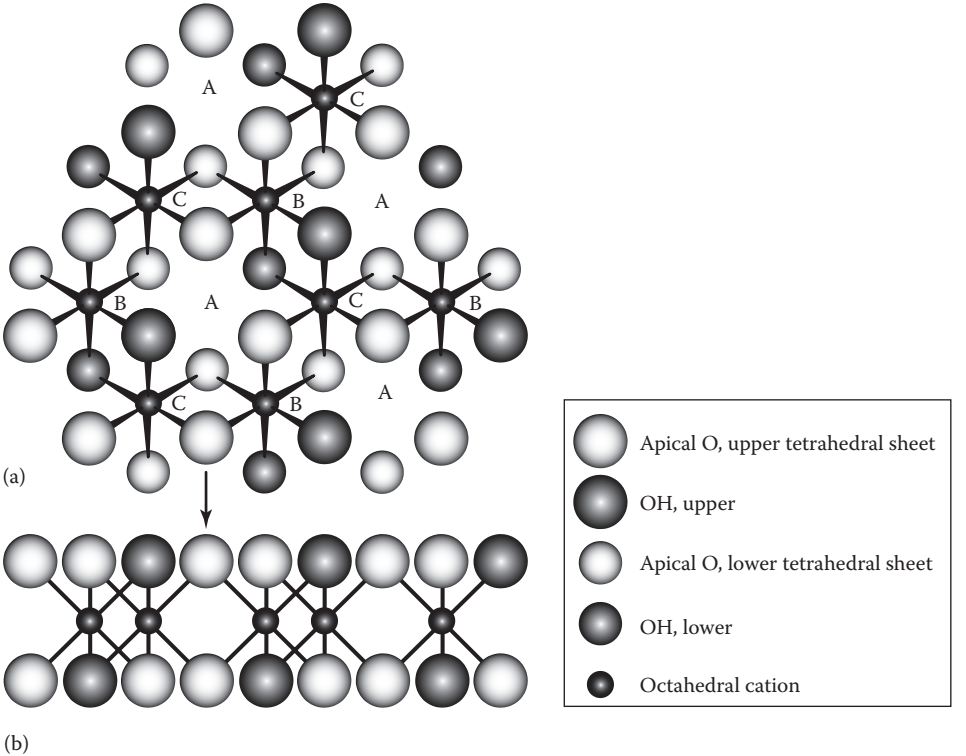


**Figure 2.18 (See color insert.)** (a) Top and (b) side views of the octahedral unit of a dioctahedral phyllosilicate mineral. The different octahedral sites are denoted as positions A, B, and C.

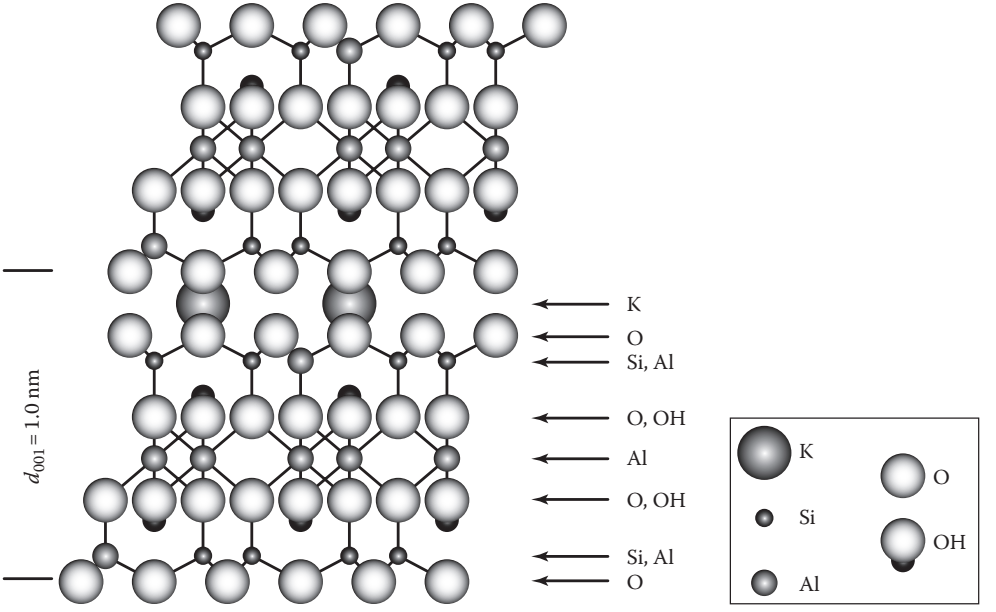


**Figure 2.19** **(See color insert.)** The structure of the dioctahedral mica muscovite ($KAl_2(Si_3Al)O_{10}(OH)_2$).

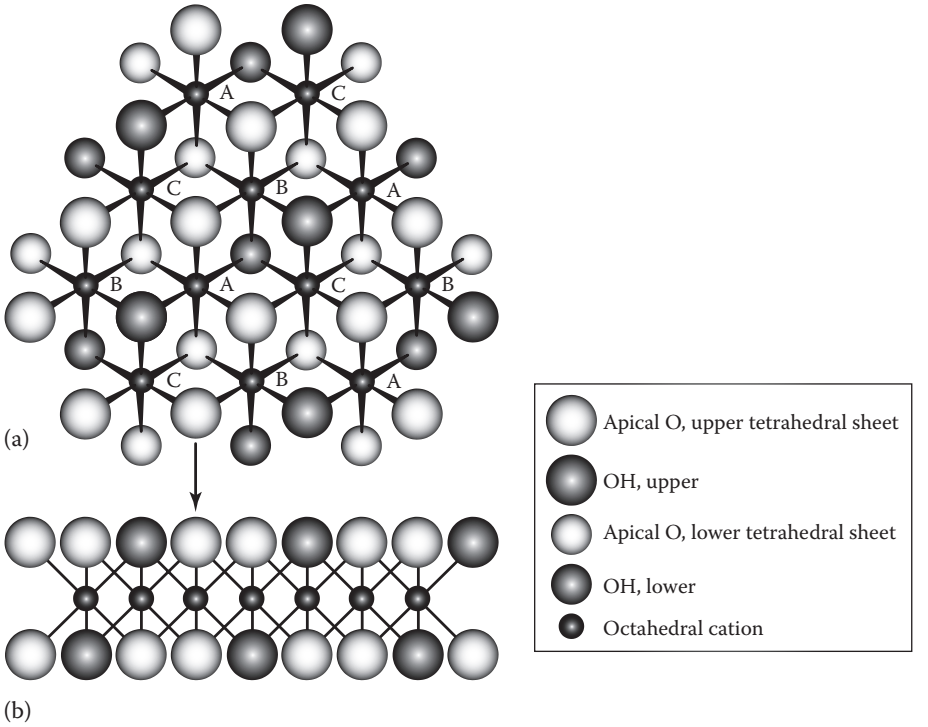


**Figure 2.20 (See color insert.)** (a) Top and (b) side views of the octahedral unit of a trioctahedral phyllosilicate mineral. The different octahedral sites are denoted as positions A, B, and C.

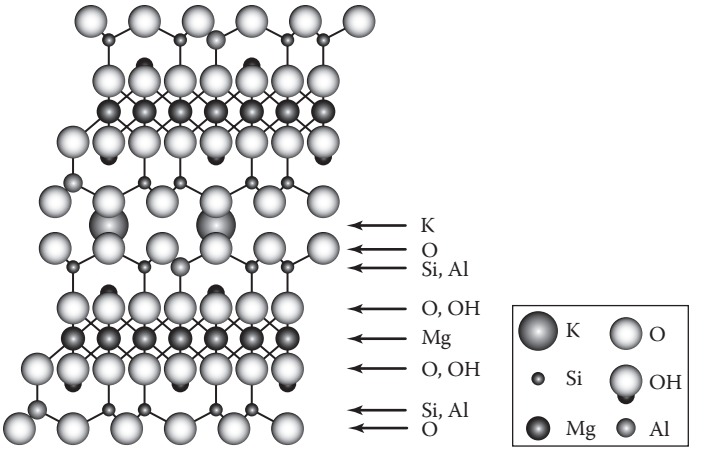


**Figure 2.21** **(See color insert.)** The structure of the trioctahedral mica phlogopite ($KMg_3(Si_3Al)O_{10}(OH)_2$).

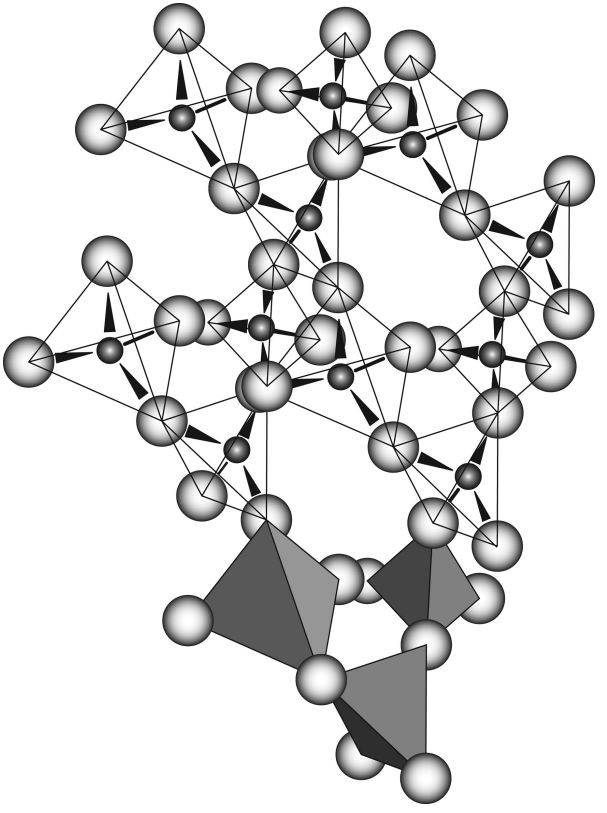

**Figure 2.22** The tectosilicate framework structure of quartz ($SiO_2$). The dark circles represent Si atoms, and the light circles are oxygen atoms.

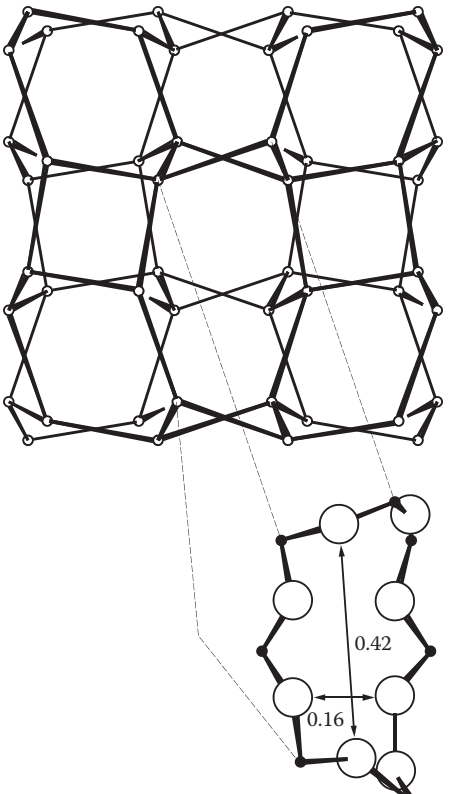


**Figure 2.23** A ball-and-stick representation of the zeolite mineral analcite ($Na_{16}(Al_{16}Si_{32})O_{96} \cdot 16H_2O$). The open circles in the main structure represent Si and Al atoms, while oxygen atoms are located at the midpoint of the connecting lines. The blown-up structure illustrates the dimensions of the channels in analcite (expressed in nanometers) and more clearly indicates the location of the oxygen atoms (open circles) in relation to the structural cations (closed circles).

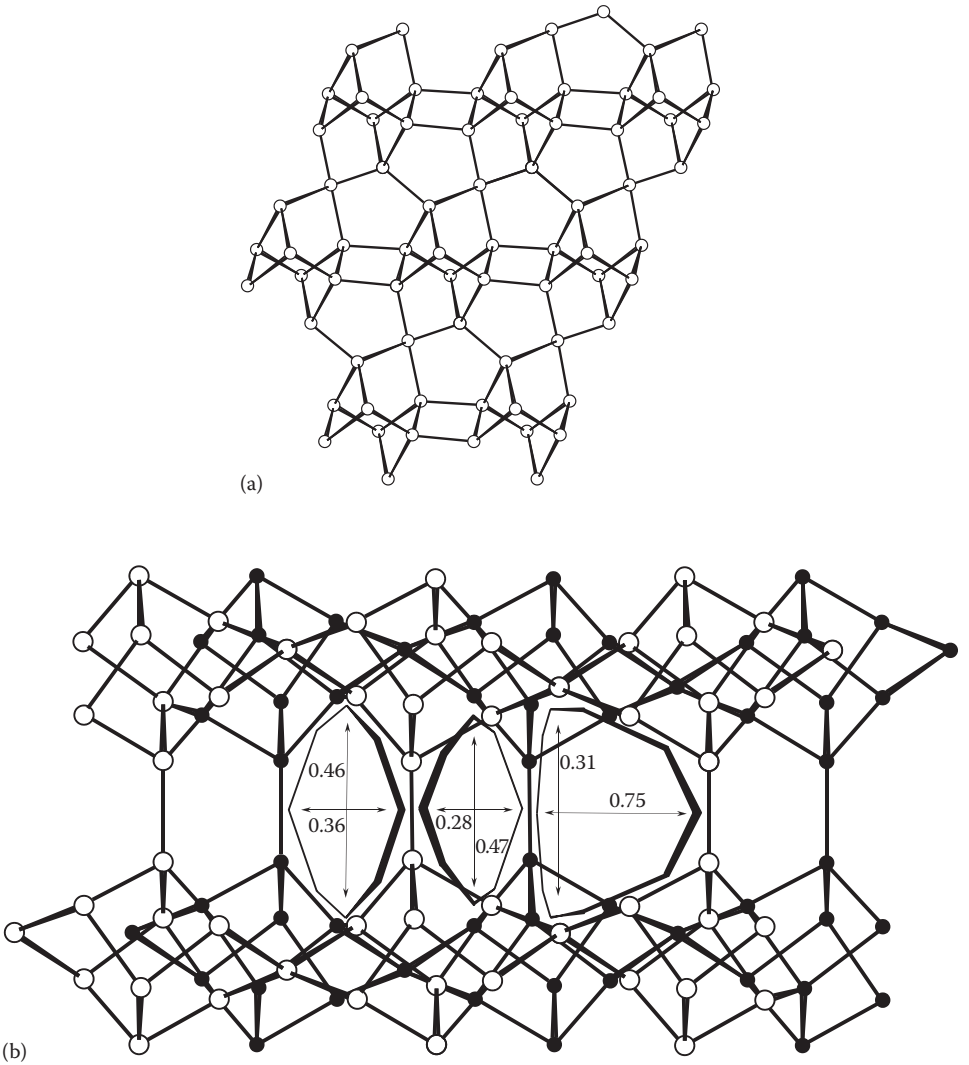


**Figure 2.24** The heulandite ($Ca_4(Al_8Si_{28})O_{72} \cdot 24H_2O$) class of zeolites, which include the clinoptilolite variety, are sheet zeolites. (a) Ball-and-stick representation of the *sheet* structure (top view, and the locations of the Si and Al atoms are represented by open circles). (b) Side view clearly showing the sheet structure as well as the dimensions (in nm) and locations of the three channel types.

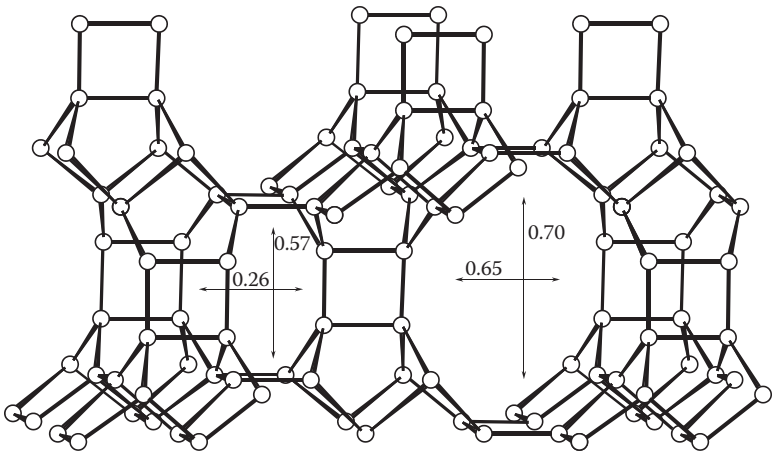


**Figure 2.25** A ball-and-stick representation of the zeolite mordenite ($Na_8(Al_8Si_{40})O_{96} \cdot 24H_2O$). The dimensions of the two types of channels in this mineral are in units of nm. Structural Si and Al atoms are represented by open circles, while oxygen atoms are located at the midpoint of the connecting lines.

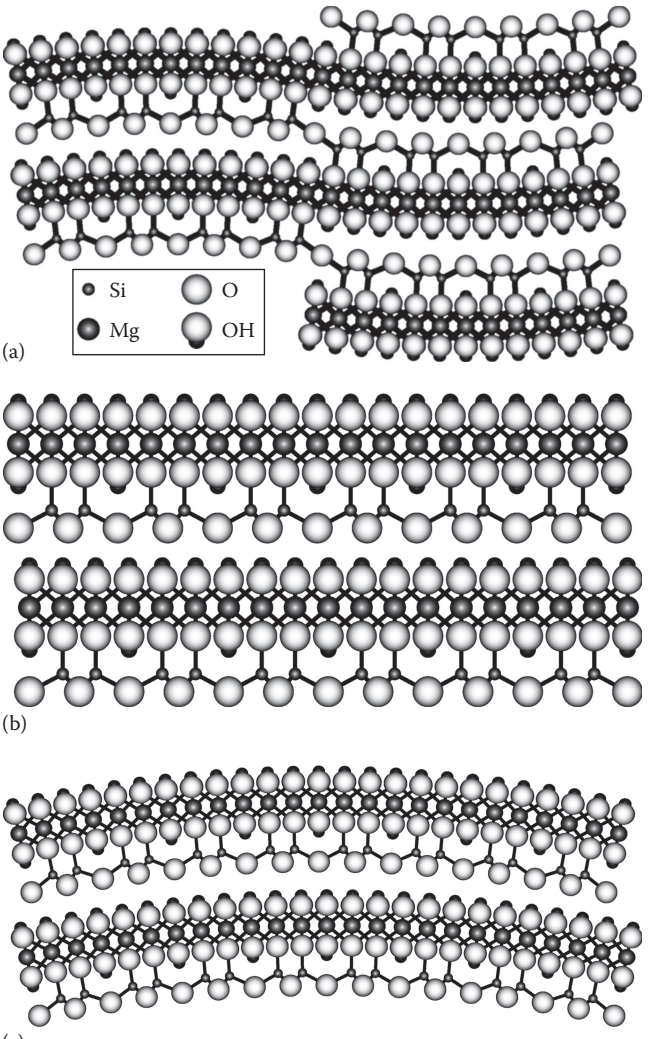


**Figure 2.26** The 1:1 structures of serpentine group minerals ($Mg_3Si_2O_5(OH)_4$). (a) The modulating wavelike structure of antigorite, (b) the planar structures of lizardite and amesite, and (c) the cylindrical roll structure of chrysolite.

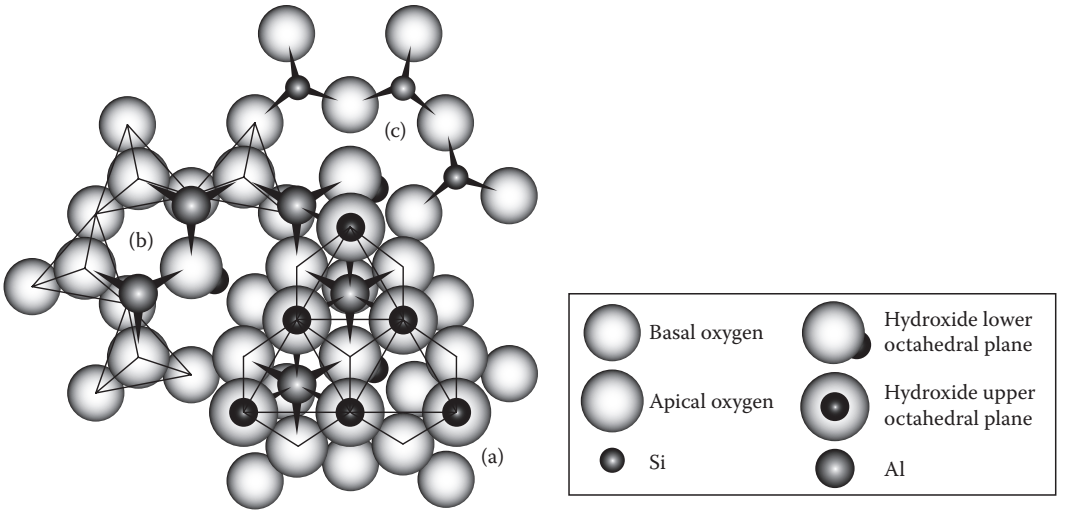


**Figure 2.27** **(See color insert.)** Representation of the spatial relationship between the Al octahedral layer (upper layer) and the distorted (ditrigonal) Si tetrahedral layer (lower layer) that occurs in the phyllosilicate minerals. a—All oxygen atoms are displayed; b—upper hydroxyl sheet removed; and c—all octahedrally coordinated anions removed.

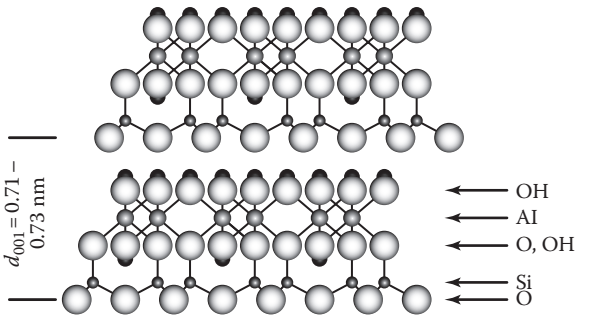


**Figure 2.28** **(See color insert.)** The 1:1 structure of kaolinite ($Al_2Si_2O_5(OH)_4$).

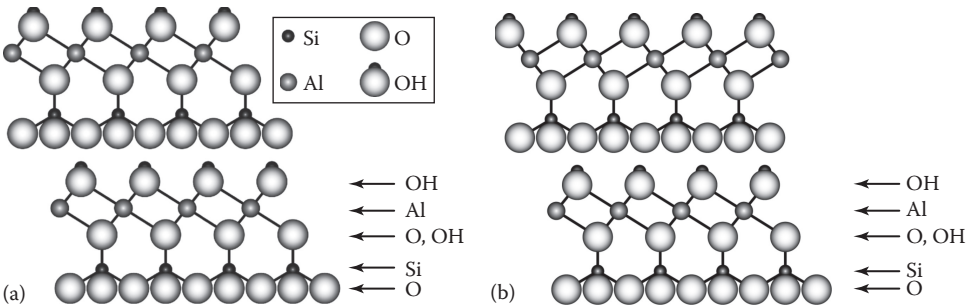


**Figure 2.29** Layer stacking in 1:1 layer silicates. (a) Adjacent octahedral layers having the same slant; (b) alternating slant of adjacent octahedral layers.

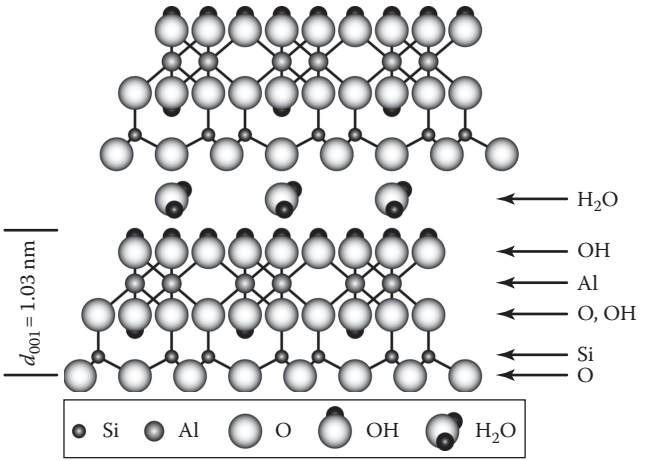


**Figure 2.30** The structure of halloysite ($Al_2Si_2O_5(OH)_4 \cdot 2H_2O$).

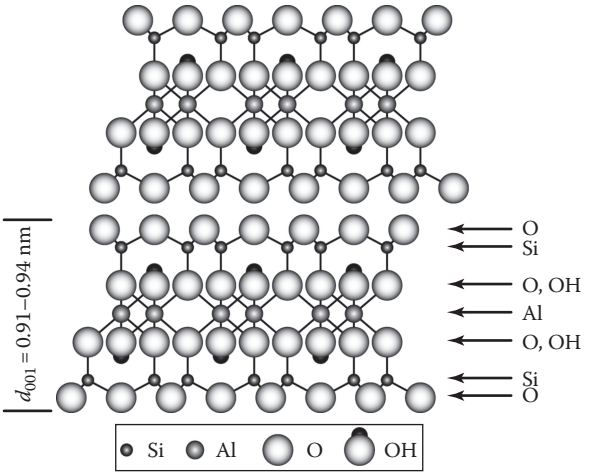


**Figure 2.31** **(See color insert.)** The structure of pyrophyllite ($Al_2Si_4O_{10}(OH)_2$).

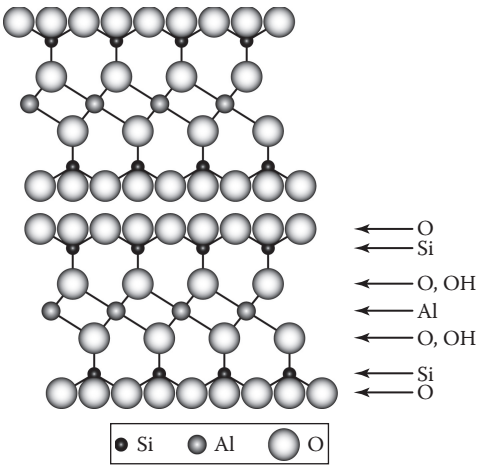


**Figure 2.32** Layer stacking in a pyrophyllite mineral with adjacent octahedral layers having the same slant.

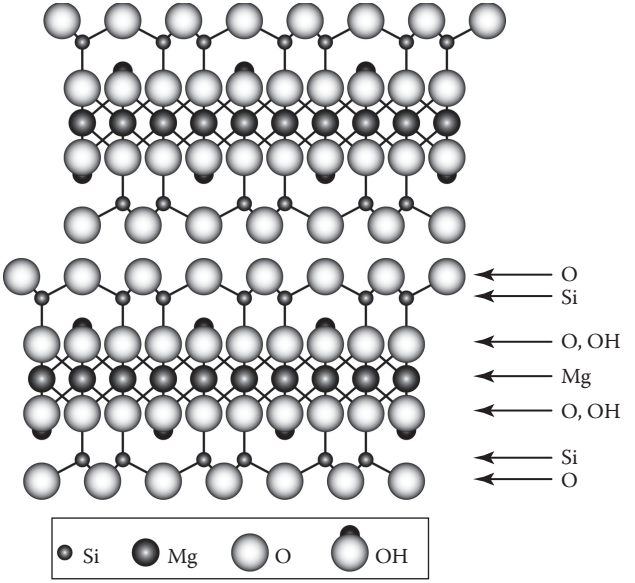


**Figure 2.33** **(See color insert.)** The structure of talc ($Mg_3Si_4O_{10}(OH)_2$).

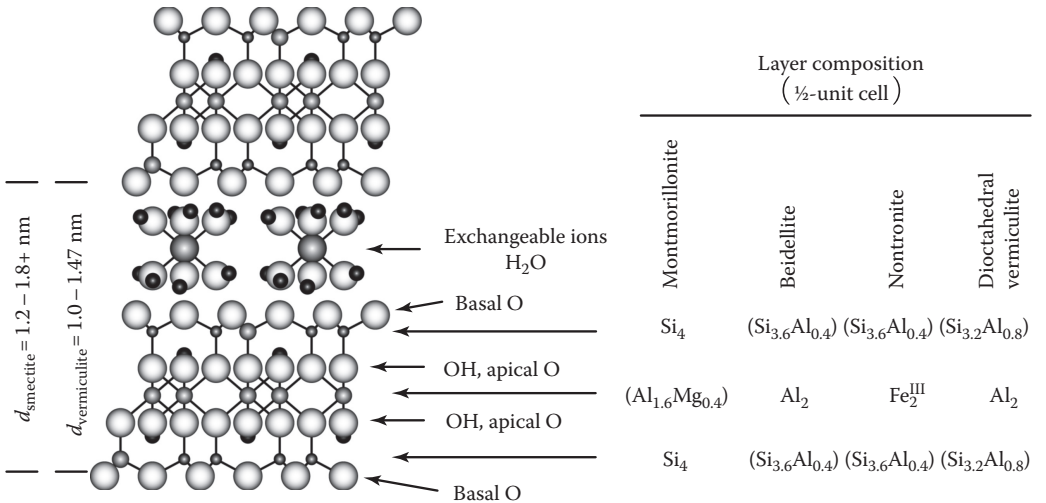


**Figure 2.34 (See color insert.)** The structural and chemical characteristics of the expandable 2:1 dioctahedral phyllosilicates montmorillonite, beidellite, nontronite, and dioctahedral vermiculite.

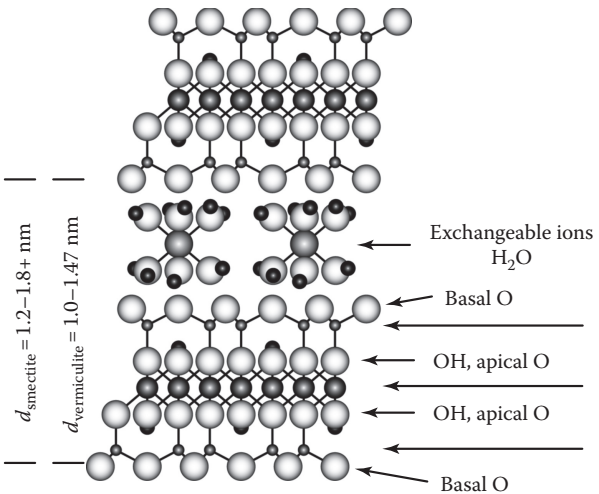


Layer composition
( ½-unit cell )

| | Hectorite | Saponite | Sauconite | Trioctahedral vermiculite |
|---|---|---|---|---|
| | $Si_4$ | $(Si_{3.6}Al_{0.4})$ | $(Si_{3.6}Al_{0.4})$ | $(Si_{3.2}Al_{0.8})$ |
| | $(Mg_{2.6}Li_{0.4})$ | $Mg_3$ | $Zn_3$ | $(Mg_{2.5}Fe_{0.5}^{III})$ |
| | $Si_4$ | $(Si_{3.6}Al_{0.4})$ | $(Si_{3.6}Al_{0.4})$ | $(Si_{3.2}Al_{0.8})$ |

**Figure 2.35 (See color insert.)** The structural and chemical characteristics of the expandable 2:1 trioctahedral phyllosilicates hectorite, saponite, sauconite, and trioctahedral vermiculite.

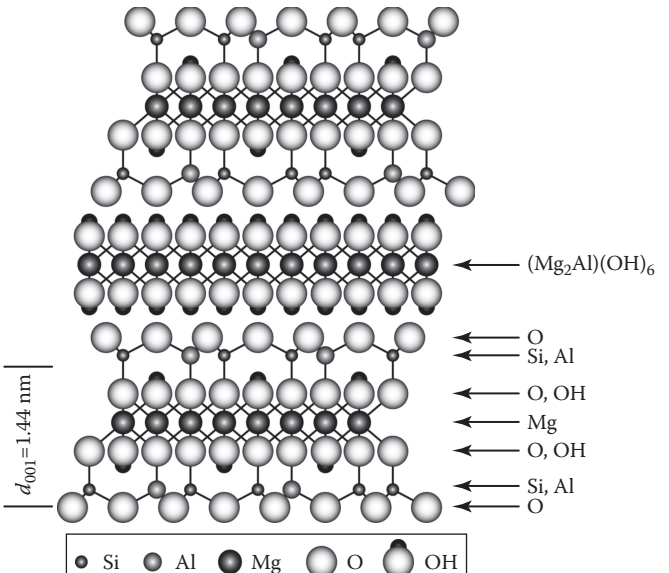


**Figure 2.36** **(See color insert.)** The ideal structure of the trioctahedral chlorite clinochlore ($(AlMg_5)(Si_3Al)O_{10}(OH)_8$).

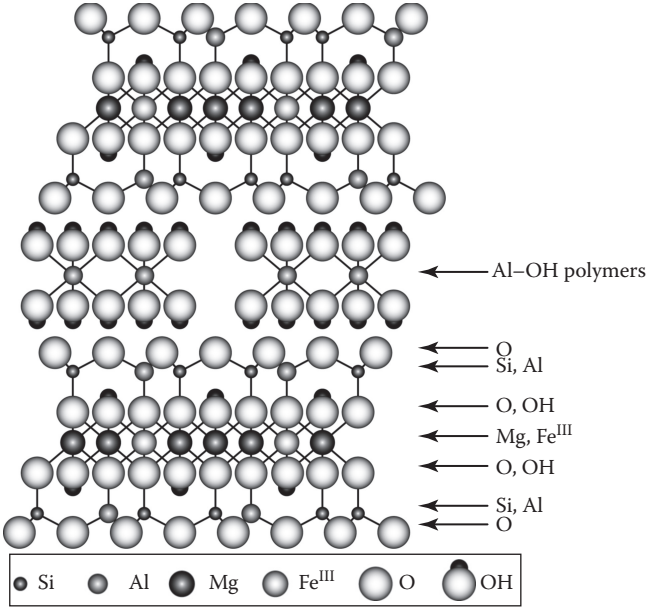


**Figure 2.37** **(See color insert.)** The structure of an HIV.

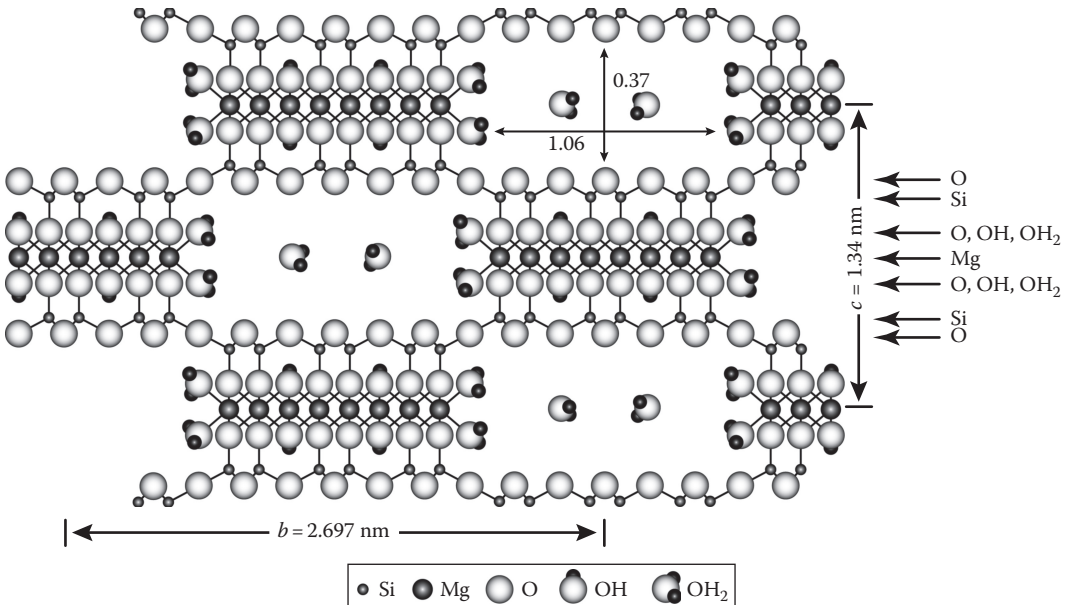


**Figure 2.38** **(See color insert.)** The structure of sepiolite $(Mg_8Si_{12}O_{30}(OH)_4(OH_2)_4(H_2O)_8)$ viewed down the *a*-axis of the unit cell. The channel dimension is in units of nm.

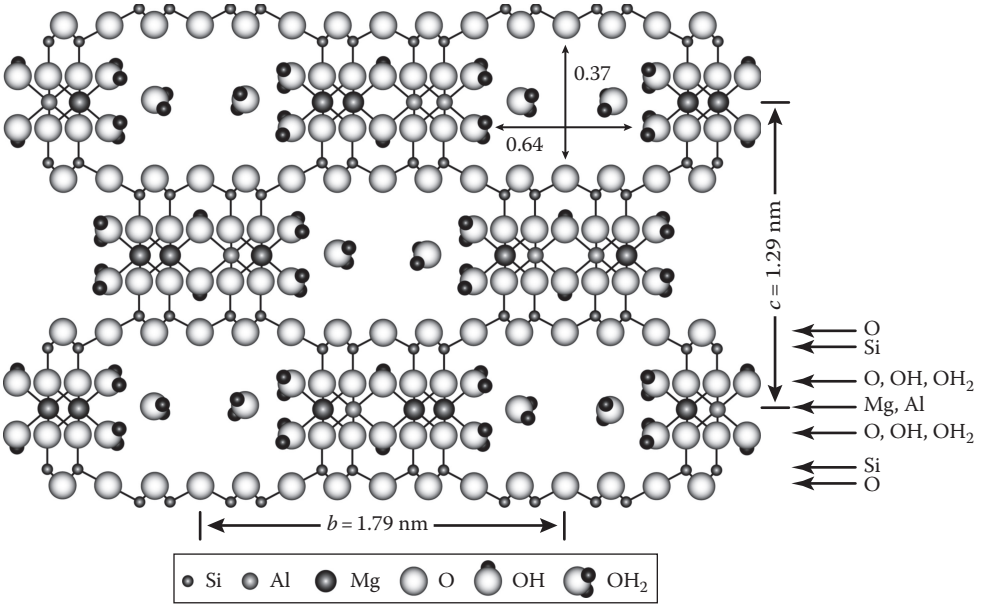


**Figure 2.39** **(See color insert.)** The structure of palygorskite ($(Mg, Al, \square)_5Si_8O_{20}(OH)_2(OH_2)_4(H_2O)_4$) viewed down the *a*-axis of the unit cell. The channel dimension is in units of nm.

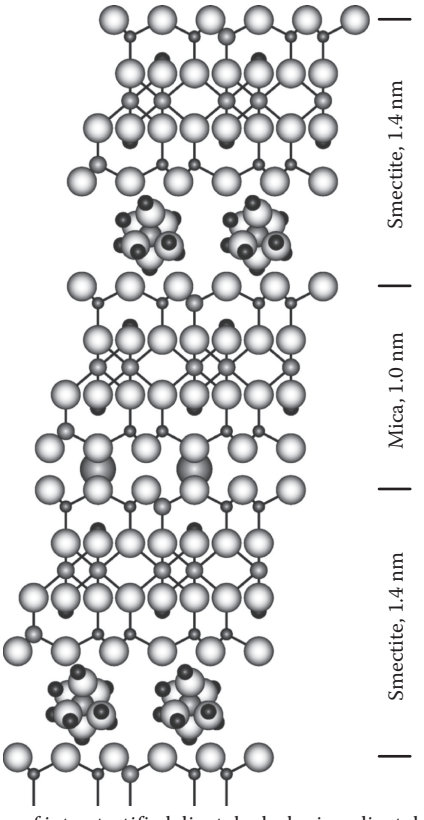


**Figure 2.40** The stacking sequence of interstratified dioctahedral mica–dioctahedral smectite.

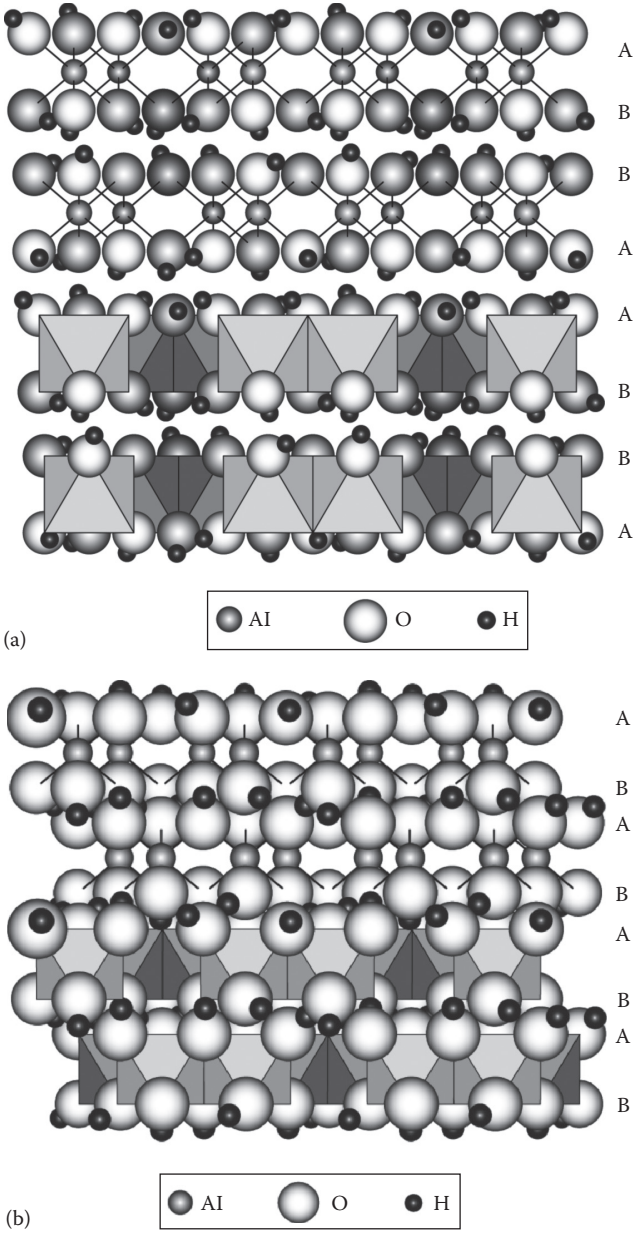


**Figure 2.41** Combined polyhedral and ball-and-stick structural models of (a) gibbsite ($Al(OH)_3$), (b) bayerite ($Al(OH)_3$). (*Continued*)

002x041a.eps

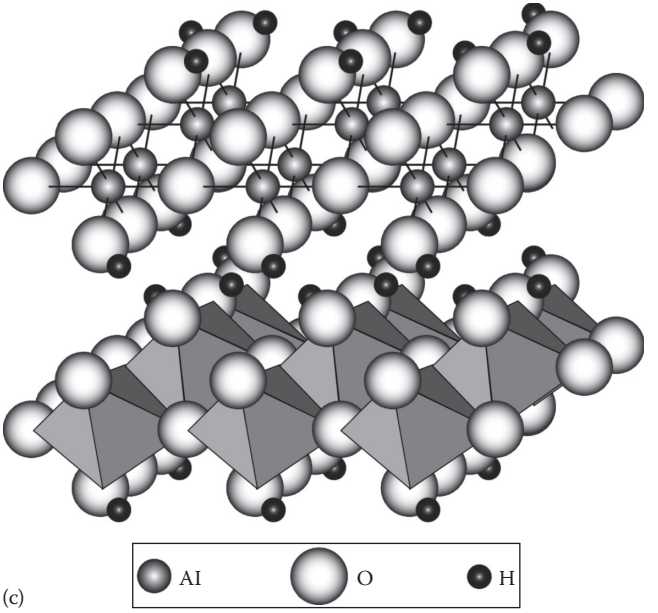


**Figure 2.41 (*continued*)** Combined polyhedral and ball-and-stick structural models of (c) boehmite (AlOOH). Lighter or larger structures are superior, while darker or smaller structures are inferior. The stacking sequences of the A- and B-type oxygen layers in gibbsite and bayerite are also illustrated.

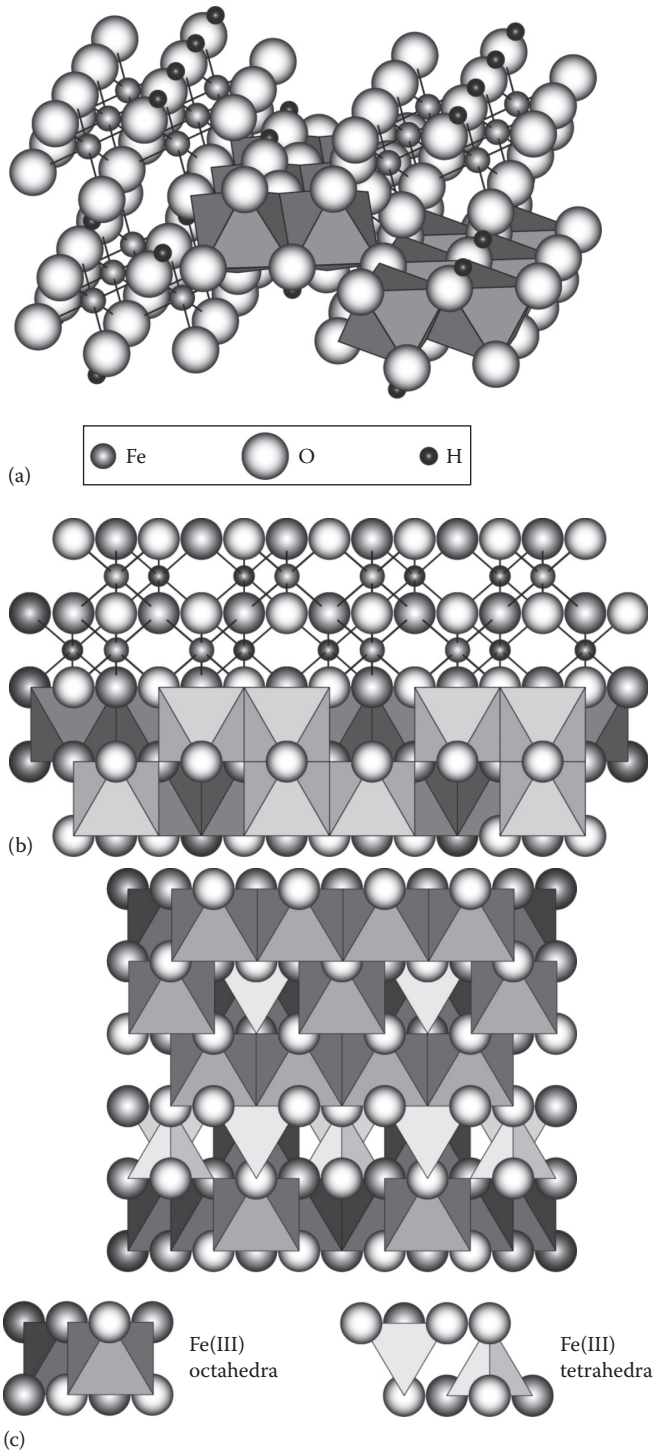


**Figure 2.42** Combined polyhedral and ball-and-stick structural models of (a) goethite (FeOOH), (b) hematite ($Fe_2O_3$), and (c) magnetite ($Fe_3O_4$) and maghemite ($Fe_2O_3$). Lighter or larger structures are superior, while darker or smaller structures are inferior.

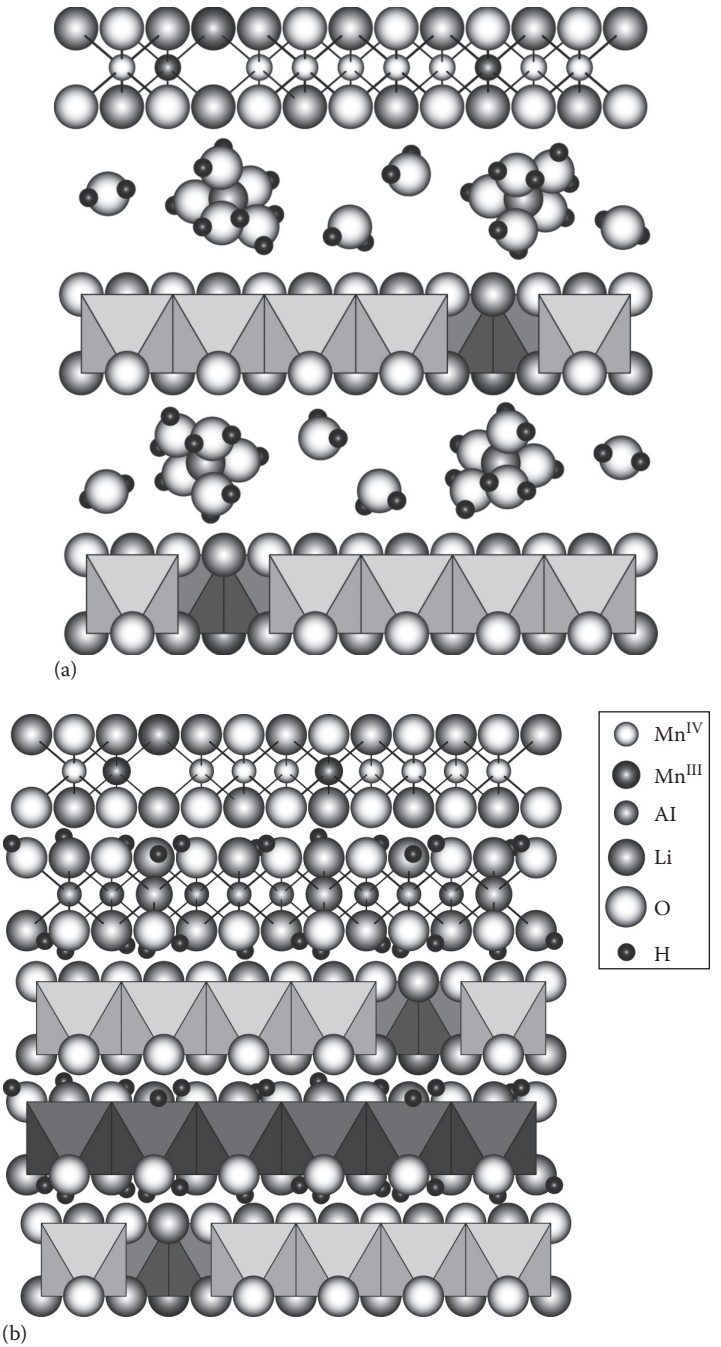


**Figure 2.43** Combined polyhedral and ball-and-stick structural models of the phyllomanganates, (a) birnessite ((Na, Ca, $Mn^{II}$)$Mn_7O_{14} \cdot 2.8H_2O$) and (b) lithiophorite ((Al, Li)$MnO_2(OH)_2$). (*Continued*)

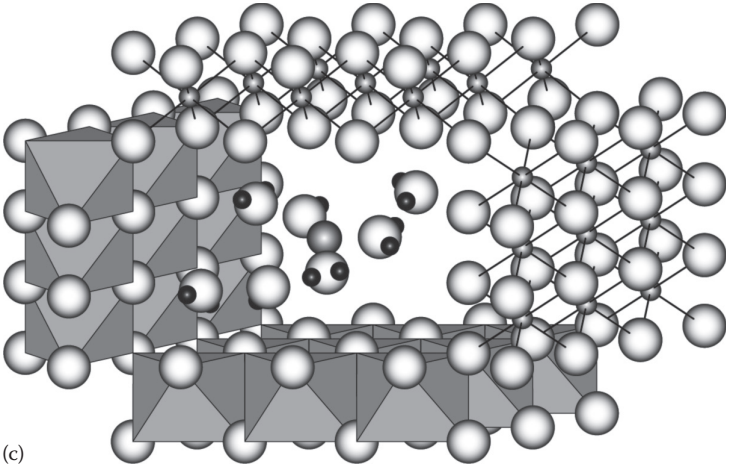


**Figure 2.43 (*continued*)** Combined polyhedral and ball-and-stick structural model of the tectomanganate, (c) todorokite ($(Na, Ca, K)_{0.3-0.5}(Mn^{IV}, Mn^{III})_6O_{12}\cdot 3.5H_2O$). Unless noted otherwise, lighter structures are superior, and darker structures are inferior.

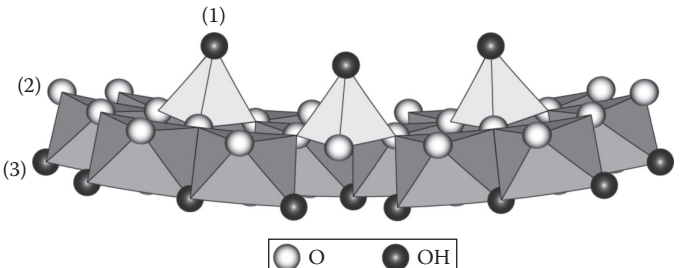


**Figure 2.44** The polyhedral structural model depicts a portion of the tubular structure of imogolite. The tube consists of three concentric anion layers: (1) the apical hydroxyls of the $Si^{4+}$ tetrahedrons pointing into the tube; (2) the basal $Si^{4+}$ tetrahedral oxygen atoms that are also common to the $Al^{3+}$ octahedrons (and reside in the interior of the tube wall); and (3) the exterior layer of $Al^{3+}$ octahedral hydroxyls.

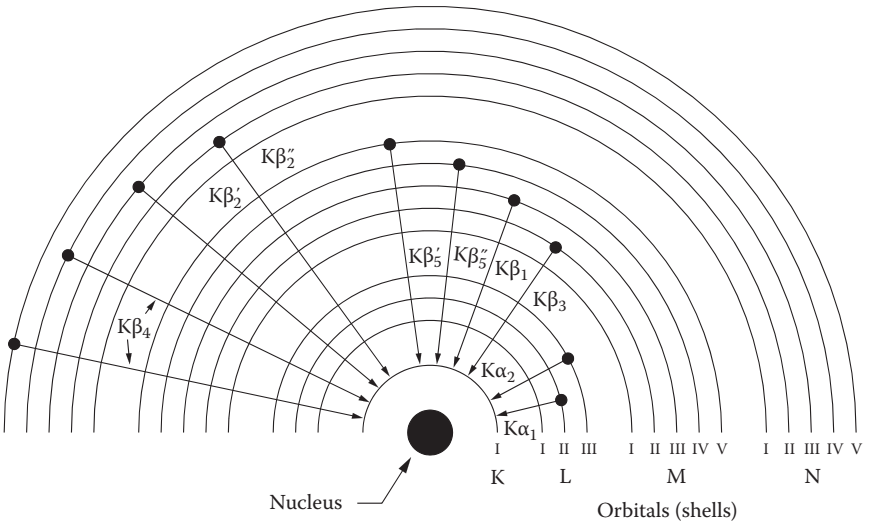


**Figure 2.45** The electronic transitions that occur when a K-shell electron is displaced, resulting in Kα and Kβ x-radiation.

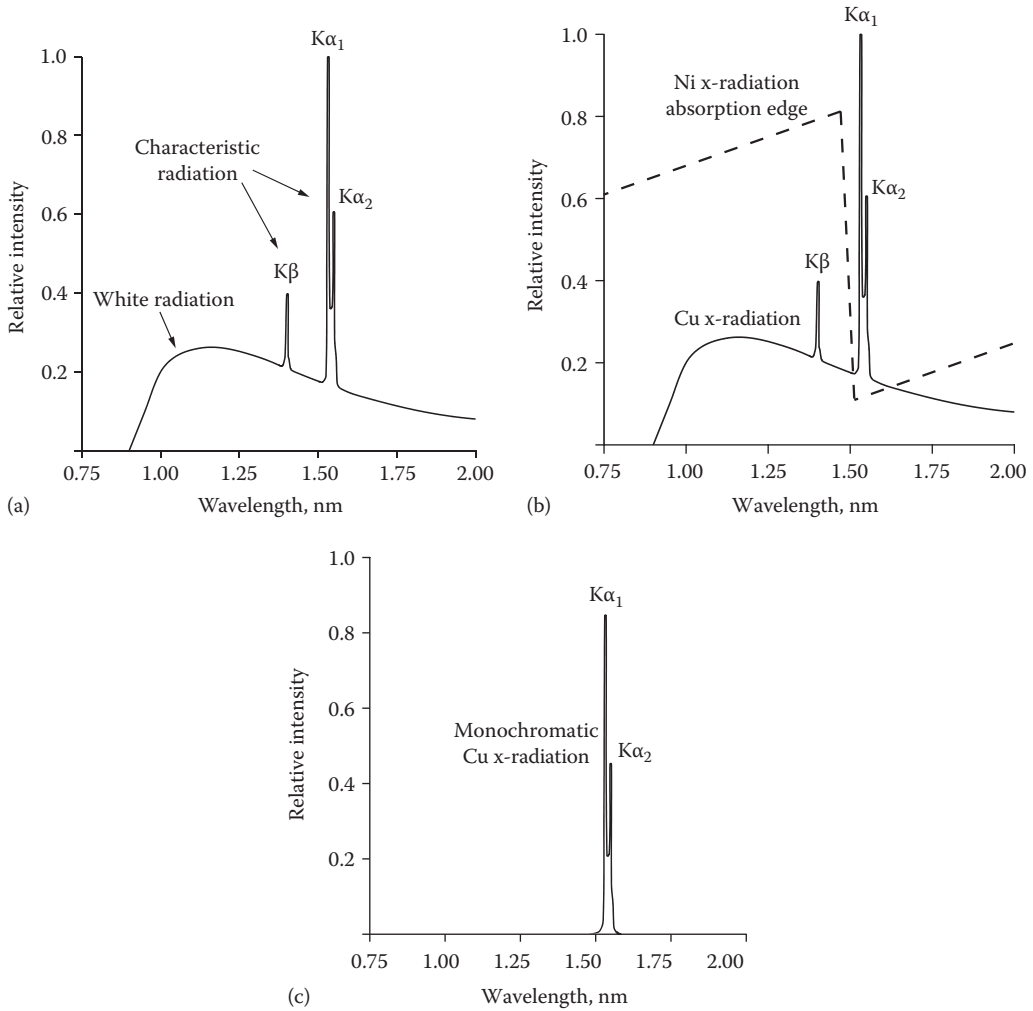


**Figure 2.46** The K-series x-ray spectrum for copper: (a) characteristic and white (heterochromatic) x-radiation emitted during the electron bombardment of Cu metal, (b) the Ni x-radiation absorption edge superimposed on the Cu spectrum, and (c) monochromatic Cu x-radiation obtained from the summation of the heterochromatic Cu x-radiation and Ni absorption edge.

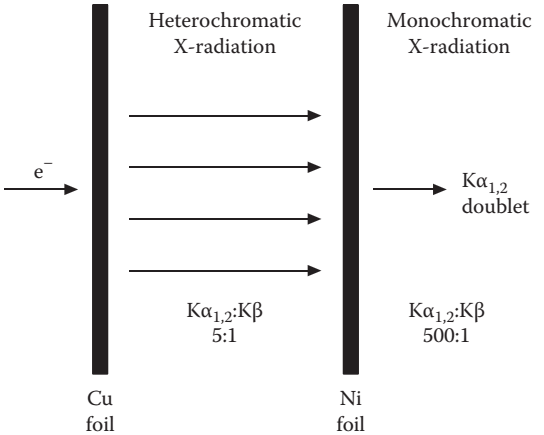


**Figure 2.47** Schematic representation of the mechanism used to produce monochromatic CuK$\alpha_{1,2}$ x-radiation.

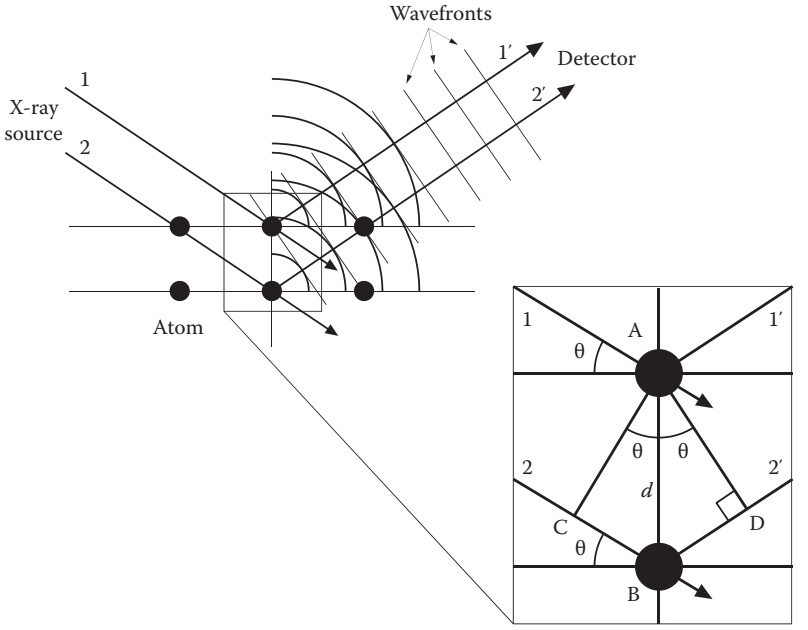


**Figure 2.48** The diffraction of x-rays by a point lattice. Incident beams 1 and 2 impact electrons that are within atoms that lie in adjacent planes of equal electronic density. The electrons radiate (diffract) x-rays 1′ and 2′. In order for 1′ and 2′ to arrive at the detector in-phase, the extra distance traveled by beam 2′ (CB + BD) must equal a multiple of the wavelength ($n\lambda$). Both triangles ABC and ABD are right triangles; therefore, CB = AB sin θ and BD = AB sin θ. It follows that (CB + BD) = 2 AB sin θ. Since (CB + BD) + $n\lambda$ and AB = $d$ (the distance between the planes of equal electronic density), $n\lambda = 2d \sin \theta$.

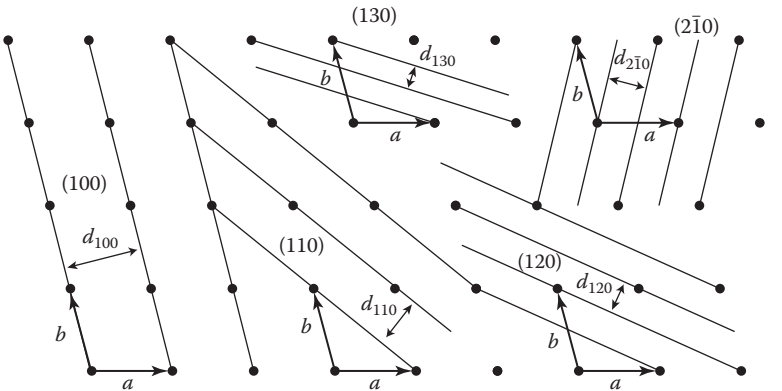


**Figure 2.49** A plane lattice (set of lattice points that are perpendicular to the *c*-axis) and example planes of equal atomic density that are parallel to the *c*-axis. The Miller indices associated with each set of planes are indicated, as is the *d*-value (the *a* and *b* vectors represent unit cell dimensions).

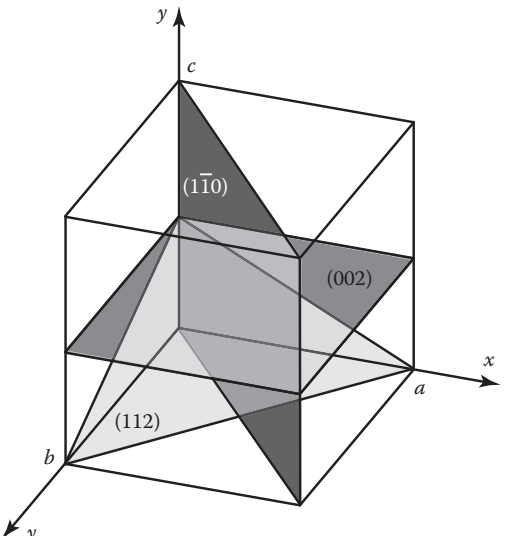


**Figure 2.50** Example planes of equal atomic density, and their associated Miller indices, for a 3D space lattice (*a*, *b*, and *c* represent the unit cell dimensions).

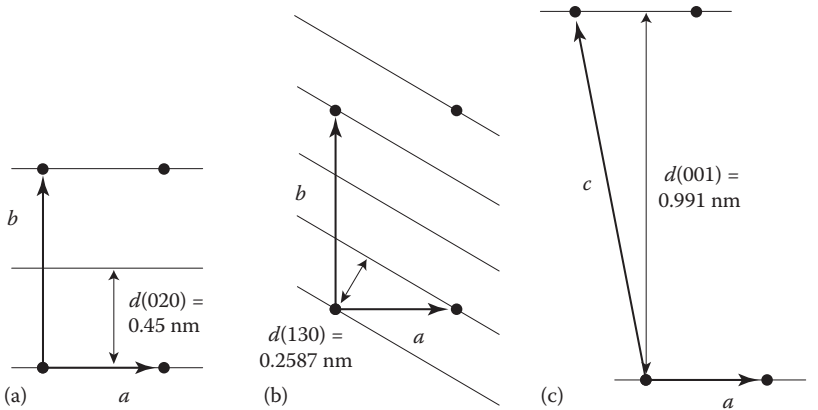


**Figure 2.51** Selected *d*-values for a muscovite-1$M_1$ (monoclinic polytype) with β = 101.00° are *d*(001) = 0.991 nm, *d*(020) = 0.450 nm, and *d*(130) = 0.2587 nm. In (a), the 020 plane is parallel to both the *a*- and *c*-axes and intersects the *b*-axis at ½*b* (*b* = 0.9 nm). In (b), the 130 plane intersects the *b*-axis at ⅓*b* and the *a*-axis at *a*. The angle at which the 130 plane intersects the *a*-axis at *a* is 30.42° (*a* is 0.511 nm). In (c), the *c*-axis dimension is 1.01 nm, computed from the *d*(001) = 0.991 nm length and the angle between the *c*-axis and the perpendicular (11°). The unit cell parameters for the muscovite-1$M_1$ polytype are *a* = 0.511 nm, *b* = 0.9 nm, *c* = 1.01 nm, and β = 101.00°.


**Figure 2.52** The two ideal orientations of clay particles for x-ray diffraction analysis: oriented, where the clay platelets lie parallel to the support structure such that the *c*-axis is preferentially presented to the x-ray beam, or random, where all planes of equal electronic density within a mineral have an equal opportunity to register a detector response (neither orientation can be achieved completely, only approached).

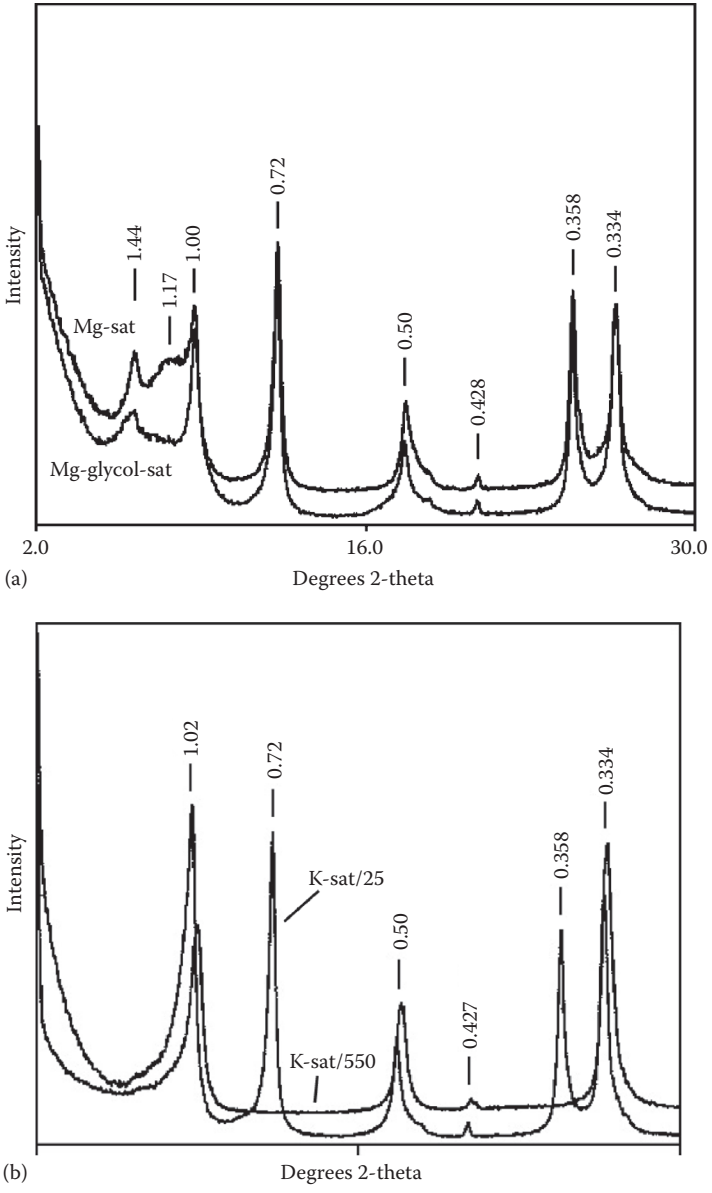


**Figure 2.53** X-ray diffractograms of clay-sized materials separated from an abandoned mine spoil material: (a) $Mg^{2+}$ and $Mg^{2+}$-glycol saturated and (b) $K^{+}$ saturated (25°C and 550°C). Peaks are identified by *d* spacing (in nm).

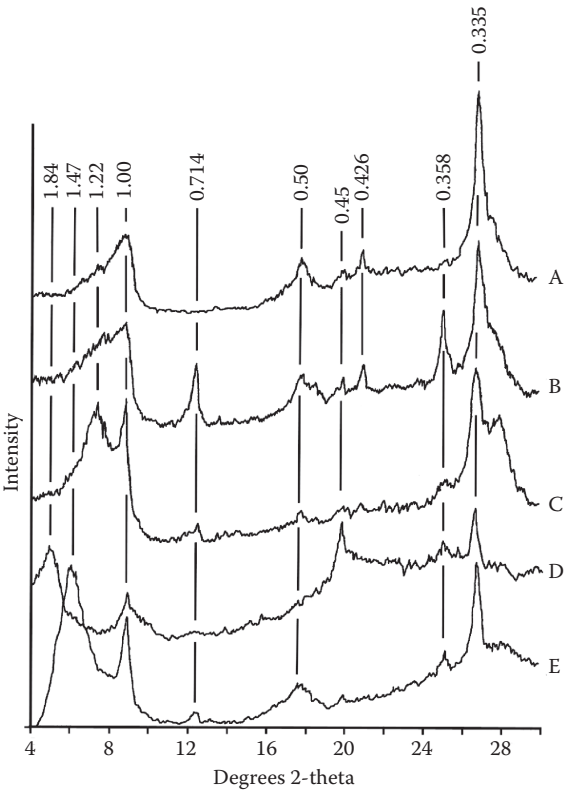


**Figure 2.54** X-ray diffractograms of the clay fraction of a San Emigdio soil. A—$K^+$ saturated, 550°C; B—$K^+$ saturated, 300°C; C—$K^+$ saturated, 25°C; D—$Mg^{2+}$ and glycerol saturated; E—$Mg^{2+}$ saturated. Peaks are identified by *d* spacing (in nm).

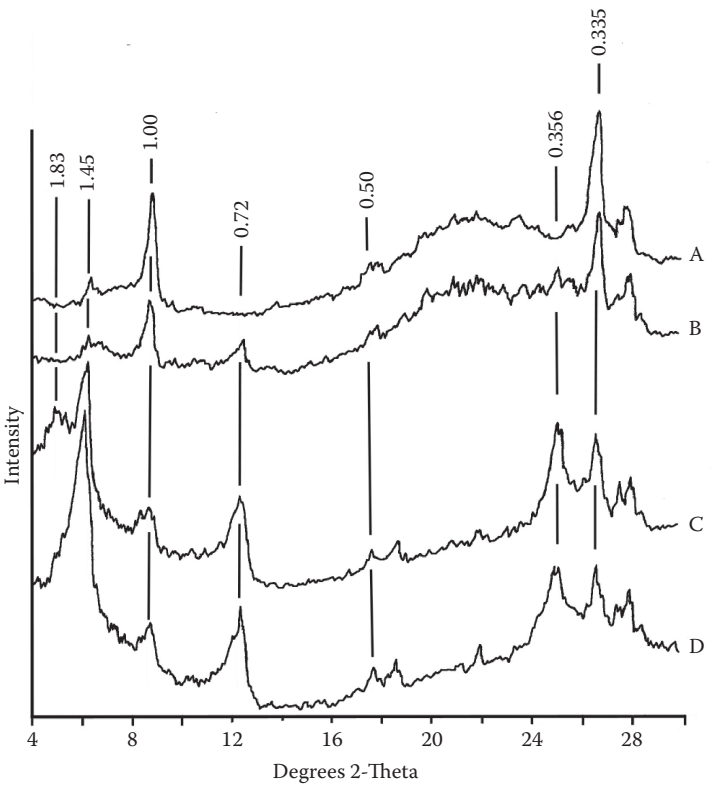


**Figure 2.55** X-ray diffractograms of the clay fraction of a Delhi soil. A—$K^+$ saturated, 600°C; B—$K^+$ saturated, 25°C; C—$Mg^{2+}$ and glycerol saturated; D—$Mg^{2+}$ saturated. Peaks are identified by *d* spacing (in nm).

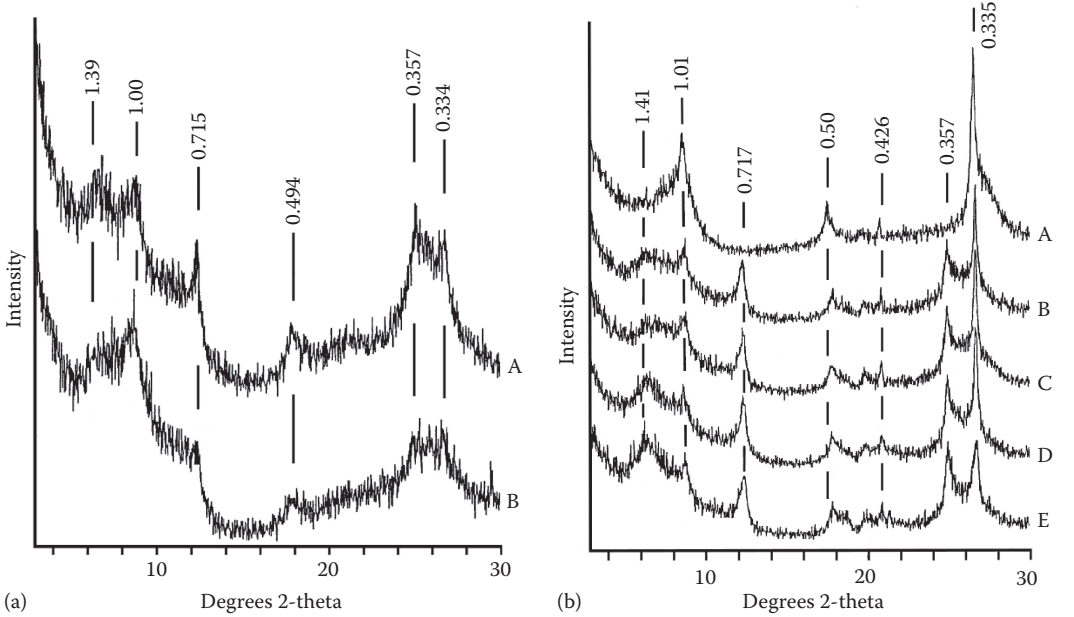


**Figure 2.56** X-ray diffractograms of the clay fraction of a Loring soil. (a) $Mg^{2+}$ and glycol saturated (A) and $Mg^{2+}$ saturated (B); (b) $K^+$ saturated, 550°C (A), $K^+$ and glycerol saturated (B), $K^+$ saturated, 300°C (C), $K^+$ saturated, 105°C (D), and $K^+$ saturated, 25°C (E). Peaks are identified by *d* spacing (in nm).